



# Modeling decompression paths in a basaltic andesite magma using the nucleation and growth of plagioclase microlites

Aaron A. Marshall<sup>1,2,4</sup> · Benjamin J. Andrews<sup>3</sup>

Received: 25 March 2023 / Accepted: 5 July 2023 / Published online: 20 August 2023  
© The Author(s) 2023

## Abstract

Plagioclase microlites in a magma nucleate and grow in response to melt supersaturation ( $\Delta\phi_{\text{plag}}$ ). The resultant frozen plagioclase crystal size distribution (CSD) preserves the history of decompression pathways ( $dP/dt$ ). SNGPlag is a numerical model that calculates the equilibrium composition of a decompressing magma and nucleates and grows plagioclase in response to an imposed  $\Delta\phi_{\text{plag}}$ . Here, we test a new version of SNGPlag calibrated for use with basaltic andesite magmas and model  $dP/dt$  for the ca. 12.6 ka Curacautín eruption of Llaima volcano, Chile. Instantaneous nucleation ( $N_{\text{plag}}$ ) and growth ( $G_{\text{plag}}$ ) rates of plagioclase were computed using the experimental results of Shea and Hammer (J Volcanol Geotherm Res 260:127–145, 10.1016/j.jvolgeores.2013.04.018, 2013) and used for SNGPlag modeling of basaltic andesite composition. Maximum  $N_{\text{plag}}$  of  $6.1 \times 10^5 \text{ cm h}^{-1}$  is achieved at a  $\Delta\phi_{\text{plag}}$  of 44% and the maximum  $G_{\text{plag}}$  of  $27.4 \mu\text{m h}^{-1}$  is achieved at a  $\Delta\phi_{\text{plag}}$  of 29%. Our modeled  $\log dP/dt_{\text{avg}}$  range from  $2.69 \pm 0.09$  to  $6.89 \pm 0.96 \text{ MPa h}^{-1}$  ( $1\sigma$ ) with an average duration of decompression from  $0.87 \pm 0.25$  to  $16.13 \pm 0.29 \text{ h}$  assuming a starting pressure  $P_i$  of 110–150 MPa. These rates are similar to those derived from mafic decompression experiments for other explosive eruptions. Using assumptions for lithostatic pressure gradients ( $dP/dz$ ), we calculate ascent rates of  $< 1\text{--}6 \text{ m s}^{-1}$ . We conducted a second set of Monte Carlo simulations using  $P_i$  of 15–30 MPa to investigate the influence of shallower decompression, resulting in  $\log dP/dt_{\text{avg}}$  from  $2.86 \pm 0.49$  to  $6.00 \pm 0.86 \text{ MPa h}^{-1}$ . The  $dP/dt$  modeled here is two orders of magnitude lower than those calculated by Valdivia et al. (Bull Volcanol, 10.1007/s00445-021-01514-8, 2022) for the same eruption using a bubble number density meter, and suggests homogeneous nucleation raises  $dP/dt$  by orders of magnitude in the shallow conduit. Our modeling further supports the rapid-ascent hypothesis for driving highly explosive mafic eruptions.

**Keywords** Basaltic andesite · Plagioclase · Crystal size distribution · Crystallization time · Ascent rate · Parallelized computing

## Introduction

### Investigating magma ascent rates

Decompression rate affects eruption style (e.g., Eichelberger et al. 1986; Jaupart and Allegre 1991; Burgisser and Gardner 2005; La Spina et al. 2021; Bamber et al. 2020). As magmas ascend from depth, volatiles exsolve and crystals nucleate and grow in response to changes in pressure ( $P$ ) and temperature ( $T$ ). During rapid ascent, bubbles remain coupled to the magma resulting in explosive eruption (Eichelberger et al. 1986; Jaupart and Allegre 1991). Conversely, during slow ascent, bubbles coalesce, resulting in sufficient permeability to degas the melt and thus removes the volatile primer necessary for explosivity and results in effusive eruption (Mangan and Sisson 2000). Crystallization of microlites during

Communicated by Mark S Ghiorso.

✉ Aaron A. Marshall  
aaron\_a\_marshall@rl.gov

Benjamin J. Andrews  
andrewsb@si.edu

<sup>1</sup> Department of Geosciences, Boise State University, Boise, ID 83725, USA

<sup>2</sup> Smithsonian Institution, Washington, DC 20560, USA

<sup>3</sup> Global Volcanism Program, Smithsonian Institution, Washington, DC 20560, USA

<sup>4</sup> Present Address: Department of Regulatory Strategy and Integration, Central Plateau Cleanup Company, 2620 Fermi Ave., Richland, WA 99354, USA

decompression increases magma viscosity (Vona et al. 2011; La Spina et al. 2016; Vetere et al. 2021) and may act to either impede the ability of gas to decouple from the magma or enhance coalescence by pushing isolated vesicles together. As such, understanding the rate of magma decompression and therefore ascent rate is important for estimating eruption duration, intensity, and volcano hazards.

Several analytical and experimental methods exist for the investigation of magma decompression rate, each with their own strengths and weaknesses. Bubble and crystal textures provide a record of magma decompression or ascent path (Cashman and Marsh 1988; Blundy and Cashman 2008; Arzilli et al. 2019; Bamber et al. 2020; Marshall et al. 2022a; Valdivia et al. 2022), and thus rocks provide a valuable look into the subsurface evolution of a magma. Crystal size distributions (CSDs) of microlites can be used to approximate crystallization times when a crystal growth rate is assumed (Marsh 1988; Cashman and Marsh 1988; Murch and Cole 2019; Bamber et al. 2020; Valdivia et al. 2022). Although CSDs can be easily measured and their slopes used for interpretation of changing ascent rates, the calculations may be skewed if post-fragmentation crystallization occurs. In addition, CSDs assume constant crystal nucleation and growth rates. More sophisticated investigations involve reproducing measured microlite textures by performing magma decompression experiments (Fig. 1), during which crystal textures evolve in response to an applied perturbation in  $P$  and/or  $T$  (Geschwind and Rutherford 1995; Hammer and Rutherford 2002; Hammer 2004; Szramek et al. 2006; Castro and Dingwell 2009; Andrews and Gardner 2010; Brugger and Hammer 2010; Shea and Hammer 2013; Waters et al. 2015; Befus and Andrews 2018). Decompression experiments are effective at approximating ascent rates by producing sufficient effective undercooling ( $\Delta T_{eff}$ ) or supersaturation ( $\Delta\phi$ ) necessary to drive crystallization, but for the most part only produce time-averaged ascent rates that do not reflect possible changes in ascent rate as a magma nears the surface. Furthermore, conducting decompression experiments can be time-consuming. Mineral breakdown reaction rims (Rutherford and Hill 1993; Browne and Gardner 2006) and compositional zoning (Waters et al. 2015) form in response to the pressure change imposed on a magma during ascent but are not always present. Melt embayments allow for diffusive modeling of elemental loss and thus ascent rates (Liu et al. 2007; Myers et al. 2016, 2018; Barth et al. 2019). Melt inclusions and embayments are, however, not perfect storage containers. Mineral fractures may result in leakage, and diffusion modeling cannot be conducted without knowledge of initial conditions and diffusive boundary conditions. Finally, geophysical observations can be used to monitor seismicity with depth in real time and allows researchers to track magma movement during an eruption (e.g., Moran et al. 2008; Thelen et al. 2008). Most volcanoes, however, are not

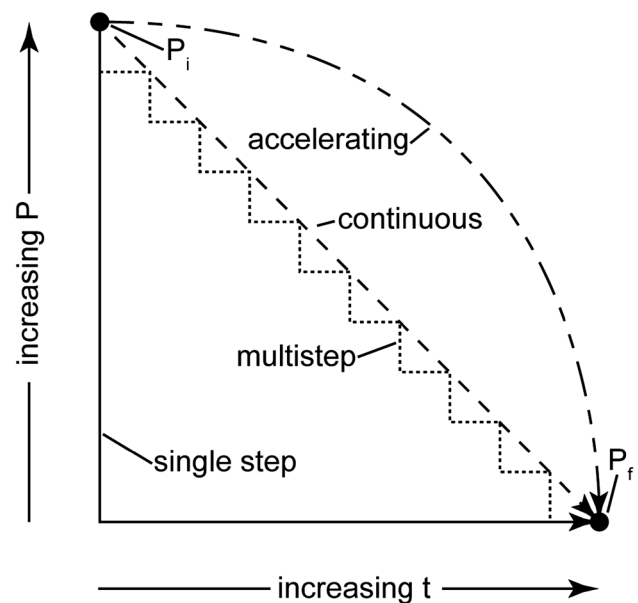


**Fig. 1** Schematic diagram of different decompression pathways. Single step experiments are subjected to a single perturbation in pressure and held at the new pressure until quenching (fragmentation). Continuous experiments undergo a continuous, uniform rate of decompression until quenching. Multistep experiments are subjected to different decompression events and pauses leading up to quenching. Accelerating experiments are subject to an increasing decompression rate over time. The crystal textures produced during decompression are quantified to compare with natural crystal textures to estimate natural decompression rates

equipped with extensive geophysical arrays that allow precision monitoring, and geophysical observations may not distinguish between different types of subsurface volcanic activity.

### Existing numerical models for magma ascent rate

To circumvent some of the disadvantages of existing experimental and analytical methods for investigating ascent rates, numerical models exist that utilize observations easily collected from rocks. Toramaru (2006) developed a magma ascent rate meter as a function of bubble number density (BND) assuming a single homogeneous nucleation event and constant decompression. Although BNDs indeed reflect changes in volatile supersaturation and decompression, extensive coalescence, multiple nucleation events, highly tortuous bubble networks (e.g., Valdivia et al. 2022), or collapsed foam textures are not representative of original BNDs and will skew ascent rate calculations. The model of Toramaru et al. (2008) uses microlite number densities (MND) to estimate ascent rates and only requires water and groundmass Si content at the point of microlite nucleation as additional inputs. But as Murch and Cole (2019) point out, the model results of Toramaru et al. (2008) are highly

influenced by the Si content input, and an error of only 5% in Si content can result in errors in ascent rate calculations as large as 500%. In addition, both models only produce time-averaged ascent rates rather than instantaneous rates over time, and therefore do not adequately model variable ascent rates that occur in nature (e.g., Mastin and Ghiorso 2000; Moran et al. 2008; Thelen et al. 2008). More recent numerical models consider the fluid dynamics of three phase basaltic magmas and disequilibrium crystallization and vesiculation during their ascent (La Spina et al. 2016; Arzilli et al. 2019; La Spina et al. 2021; Bamber et al. 2020).

## SNGPlag

Supersaturation Nucleation and Growth of Plagioclase (SNGPlag) is an iterative forward model that calculates time-dependent plagioclase crystallization, the integral of nucleation and growth, within a constant magma composition for a specified pressure–temperature–time ( $P$ – $T$ – $t$ ) path (Andrews and Befus 2020). Comprehensive descriptions of the model can be found in Befus and Andrews (2018) and Andrews and Befus (2020) and are only summarized here. Specifically, the model tracks the numbers and sizes of plagioclase crystals within a 1 m<sup>3</sup> volume of magma. SNGPlag considers nucleation and growth as functions of plagioclase supersaturation ( $\Delta\phi_{\text{plag}}$ ), defined as the difference between the equilibrium volume fraction of plagioclase as determined using MELTS (Gualda et al. 2012; Ghiorso and Gualda 2015) and the modeled volume fraction. SNGPlag uses  $\Delta\phi_{\text{plag}}$  rather than  $\Delta T_{\text{eff}}$  as the former can be readily determined through time whereas  $\Delta T_{\text{eff}}$  is only known at the onset of decompression. Melt decompression and/or cooling act to increase  $\Delta\phi_{\text{plag}}$ . Nucleation and growth of plagioclase crystals in response to  $\Delta\phi_{\text{plag}}$  drive the magma towards equilibrium, with the instantaneous nucleation and growth rates of plagioclase being functions of  $\Delta\phi_{\text{plag}}$  (Befus and Andrews 2018). SNGPlag allows nucleation and growth to be path-dependent and does not assume constant nucleation and growth rates (Andrews and Befus 2020). SNGPlag can model multiple styles of decompression (e.g., linear, accelerating, paused) to investigate the style of decompression on plagioclase crystallization. Multiple decompression styles may be applied to the same simulation, such as a linear pathway that has a pause during decompression. While SNGPlag cannot provide a unique solution for natural samples, it can describe a limited range of likely decompression rates and paths (Andrews and Befus 2020).

Previous versions of SNGPlag are calibrated for felsic compositions. Here, we extend the calibration of SNGPlag to include basaltic andesite compositions using the experimental results of Shea and Hammer (2013). We then apply an inverse implementation of SNGPlag to the 12.6 ka basaltic andesite Curacautín eruption of Llaima volcano, Chile (Marshall et al.

2022a; Valdivia et al. 2022) to estimate decompression rates necessary to generate ignimbrite-forming mafic eruptions. The results and application of our modeling can be applied to similar mafic volcanic centers to investigate the conditions that result in unusually explosive mafic eruptions.

## The Curacautín eruption

The Curacautín eruption occurred at ca. 12.6 ka and resulted in the deposition of the extensive Curacautín ignimbrite (Ci, Marshall et al. 2022a). The Ci is a 4.0–4.5 km<sup>3</sup> (dense-rock equivalent) unconsolidated basaltic andesite ignimbrite exposed radially around Llaima that flowed up to 30 km from Llaima (Marshall et al. 2022a; Naranjo and Moreno 2005), though others have mapped the Ci up to 100 km from source (Naranjo and Moreno 1991). The Ci consists of four coarse ash to fine lapilli tuff flow units (Fig. 2, Marshall et al. 2022a). Recent work by Marshall et al. (2022a) and Valdivia et al. (2022) suggests the Ci is the result of fragmentation of a rapidly ascending, non-degassed magma at a low fragmentation threshold. There is no evidence to suggest the explosivity of the Ci eruption was driven by magma–water interaction, though some evidence exists for localized phreatic activity (Marshall et al. 2022a, b).

## Methods

### Calibration of SNGPlag for basaltic andesite compositions

Previously published versions of SNGPlag (Befus and Andrews 2018; Andrews and Befus 2020) use nucleation and growth rates determined experimentally for the 1991 Pinatubo dacite magma with a rhyolitic melt composition. Application of SNGPlag to the Curacautín eruption necessitates acquiring plagioclase nucleation ( $N_{\text{plag}}$ ) and growth rates ( $G_{\text{plag}}$ ) for a basaltic andesite magma. We used the results of single step decompression experiments conducted by Shea and Hammer (2013) on the Mascota basaltic andesite. Their study includes 11 experimental runs (Table 1) with  $P$ ,  $T$ ,  $\text{H}_2\text{O}$ , and compositional conditions reasonable for the Curacautín eruption (Lohmar 2008; Schindlbeck et al. 2014). Importantly, they report the plagioclase crystallinities, maximum lengths, and volumetric number densities for all runs, thereby enabling calculation of instantaneous nucleation and growth rates.

### Determination of instantaneous nucleation and growth rates of plagioclase

We adapted the existing SNGPlag code written in MATLAB to find  $N_{\text{plag}}$  and  $G_{\text{plag}}$  that best fit the experimental observations of Shea and Hammer (2013). Briefly, we assume



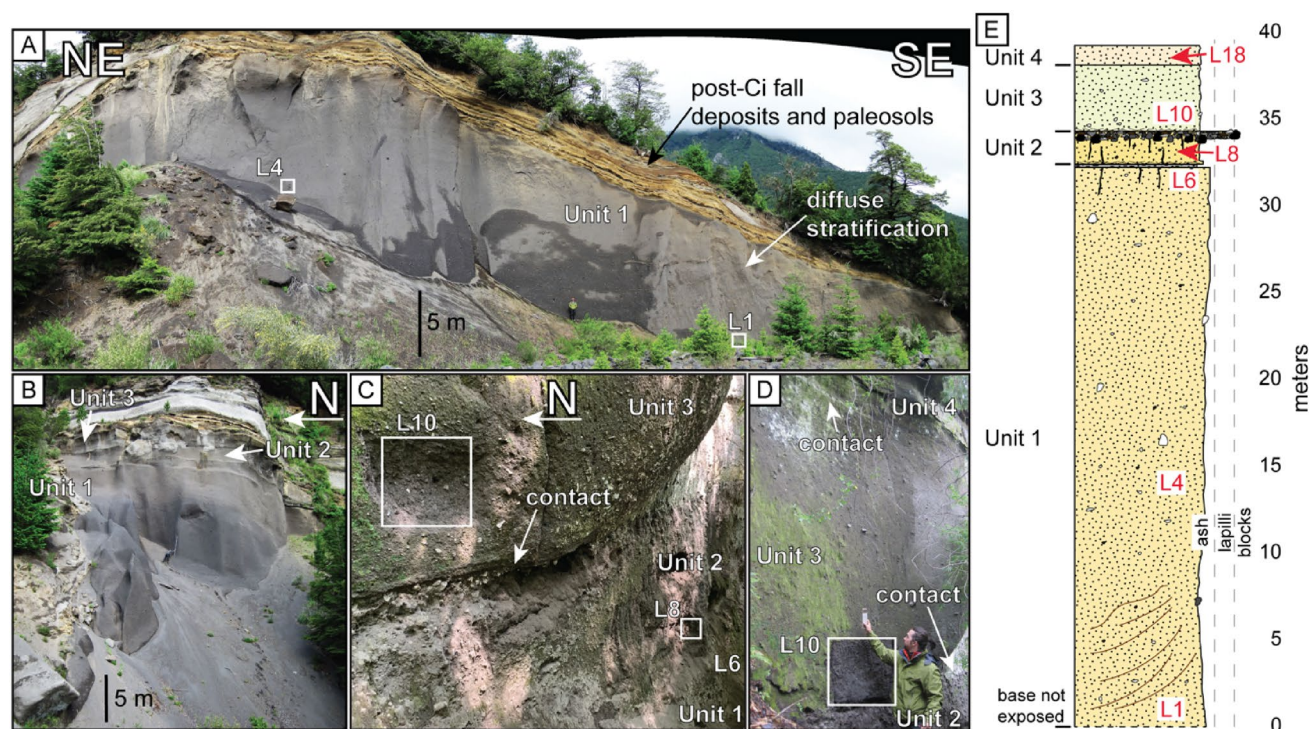


**Fig. 2** Curacautín ignimbrite flow units and eastern stratigraphy from Marshall et al. (2022a). Samples used for SNGPlag calibration and modeling come from these exposures. **A** Unit 1 where samples L1 and L4 were collected. **B** The contact between Units 1, 2, and 3 where samples. **C** Contacts between Units 1, 2, and 3 where samples

L6, L8, and L10 were collected. **D** Contacts between Units 2, 3, and 4 where L8, L10, and L18 were collected. **E** The most complete section of Ci stratigraphy measured across the eastern outcrops in A–D. Sample locations in the stratigraphic column are in red

**Table 1** Experimental conditions of Shea and Hammer (2013) used for SNGPlag calibration. Initial pressure,  $P_i$ , for all runs was 150 MPa and all runs were isothermal, with  $T_i = T_f = 1025$  °C.  $\Delta T_{eff}$  is reported as the initial plagioclase supersaturation immediately after decompression. Note that only two experiments were conducted to  $P_f < 42$  MPa

Experiment	$P_f$ (MPa)	$t$ (h)	$\Delta T_{eff}$ (°C)
SSD_52-12	100	12	52
SSD_82-12	65	12	82
SSD_112-12	42	12	112
SSD_52-24	100	24	52
SSD_82-24	65	24	82
SSD_112-24	42	24	112
SSD_52-48	100	48	52
SSD_82-48	65	48	82
SSD_112-48	42	48	112
SSD_137-48	22	48	137
SSD_155-48	10	48	155

that the  $N_{plag}$  and  $G_{plag}$  have functional forms that can be described as log-normal functions of  $\Delta\phi_{plag}$ ; variation of four different parameters can change the functional form to virtually any arbitrary path (Befus and Andrews 2018). We

find the best fit for  $N_{plag}$  and  $G_{plag}$  by running SNGPlag for the known decompression experiments of Shea and Hammer (2013) across an 8-dimensional space (four dimensions for both  $N_{plag}$  and  $G_{plag}$ ). This results in 100,000 possible combinations of  $N_{plag}$  and  $G_{plag}$ .  $N_{plag}$  and  $G_{plag}$  were modeled using the R2 high performance computing cluster at Boise State University. The best fit  $N_{plag}$  and  $G_{plag}$  are those that best recover the observed results of Shea and Hammer (2013). Run parameters were taken from Shea and Hammer (2013) with each single-step run discretized into 2,500  $P$ – $T$ – $t$  steps.  $N_{plag}$  and  $G_{plag}$  are calculated at each step as functions of  $\Delta\phi_{plag}$  with the form:

$$\frac{k}{x\sqrt{2\pi}} \exp\left(-\frac{(\ln x - \mu)^2}{2\sigma^2}\right), \quad (1)$$

where  $x = b \cdot \exp^{\Delta\phi_{plag}}$ ,  $\Delta\phi_{plag}$  = plagioclase supersaturation, and  $\mu$ ,  $\sigma$ ,  $b$ , and  $k$  are fit parameters that describe the specific shape of curves that represent the mean, standard deviation, scaling with respect to  $\Delta\phi_{plag}$ , and its maximum value (Befus and Andrews 2018). The input ranges and best fit calibration parameters for  $N_{plag}$  and  $G_{plag}$  are provided in Table 2. Values for  $\mu$ ,  $\sigma$ , and  $k$  were randomly sampled from a selected range (Table 2). For our calibration,  $b$  was set to

**Table 2** Plagioclase nucleation ( $N_{plag}$ ) and growth ( $G_{plag}$ ) rate calculation parameters.  $\mu$ ,  $\sigma$ , and  $b$  are fitting parameters with no units.  $k$  has units of  $\text{m}^{-3} \text{s}^{-1}$  for  $N_{plag}$  and  $\text{um s}^{-1}$  for  $G_{plag}$ 

Variable	$N_{plag}$ range	Optimum $N_{plag}$	$G_{plag}$ range	Optimum $G_{plag}$
$\mu$	0.1–1.5	0.5398	0.1–1.5	0.5290
$\sigma$	0.5–2	0.5970	0.5–2	0.8770
$b$	1	1	1	1
$k$	$10^9$ – $10^{13}$	$6.0677 \times 10^9$	$10^{-10}$ – $10^{-5}$	$2.2003 \times 10^{-8}$

1. SNGPlag accounts for volume interferences  $\phi_{int}$  between crystals for a randomly distributed population of crystals by,

$$\phi_{int} = 0.5(\phi_{app})^2, \quad (2)$$

where  $\phi_{app}$  is the apparent crystallinity, which is the sum of all crystal sizes and numbers calculated at each step divided by the system volume ( $1 \text{ m}^3$ ). From this, we obtain the equation,

$$\phi_{plag} = \phi_{app} - \phi_{int}, \quad (3)$$

where plagioclase crystallinity  $\phi_{plag}$  is reported with overlapping crystals removed (Andrews and Befus 2020). Finally, uncertainty in  $N_V$  and  $\sigma_{N_V}$  is determined by,

$$\sigma_{N_V} = (SnN_V)^{-0.5}, \quad (4)$$

where  $Sn$  is the characteristic crystal size in a  $1 \text{ mm}^2$  area (Andrews and Befus 2020). Optimum values for  $G_{plag}$  and  $N_{plag}$  were determined using least squares optimization of the calibration data (Table 2).

During each step of SNGPlag, existing plagioclase grow, and new plagioclase nucleate based upon  $G_{plag}$ ,  $N_{plag}$ , and  $\Delta\phi_{plag}$ . SNGPlag produces matrices of plagioclase crystal number and size that can be binned and converted into cumulative CSDs. Because SNGPlag calculates volumetric number densities and size distributions by nucleating and growing plagioclase in a  $1\text{-m}^3$  model volume, we avoid the uncertainties that result from stereological conversions of 2D data. Use of a  $1\text{-m}^3$  model volume to effectively eliminate rounding errors and discrepancies that can occur in smaller volumes with fewer crystals.

## Modeling conditions

Modeling the Ci CSDs using the best fit  $N_{plag}$  and  $G_{plag}$  rates requires realistic or plausible values for  $P_i$ ,  $P_f$ ,  $T$ ,  $dP/dt$ , and volume fraction phenocrysts. Schindlbeck et al. (2014) calculated Ci crystallization temperatures of  $\sim 1,110 \pm 45^\circ\text{C}$  using the olivine- and clinopyroxene-liquid thermobarometer of Putirka (2008), water content of  $1.4 \pm 0.32\%$  using the plagioclase hygrometer of Lange et al. (2009), and

storage pressures between 400 and 600 MPa corresponding to depths of up to 18 km, though work by Lohmar (2008) suggests that crystallization occurred at  $\leq 7$  km. Marshall et al. (2022a) measured phenocryst content of Curacautín pyroclasts from  $< 1$  to  $\sim 3.5\%$ , and Lohmar (2008) measured up to 7% phenocrysts. Valdivia et al. (2022) estimated  $dP/dt$  for the Ci from 0.36 to  $2.6 \text{ MPa s}^{-1}$  using the bubble number density decompression rate meter of Toramaru (2006). Finally, experiments by Arzilli et al. (2019) found the conditions required for basaltic magmas to erupt as high explosivity events are temperatures  $< 1100^\circ\text{C}$ , syn-eruptive crystal content  $\geq 30\%$ , and melt viscosities of  $10^5 \text{ Pa s}$ .

Our modeling consisted of 100,000 simulations with initial and final conditions selected in a random Monte Carlo scheme from a range of defined inputs (Table 3). We conducted experiments with  $P_i$  between 110 and 150 MPa due to the limited range of experimental pressure data used for SNGPlag calibration. We did not assume a 400–600 MPa  $P_i$  because those pressures calculated by Schindlbeck et al. (2014) are total pressure whereas those of SNGPlag are the partial pressure of water (e.g.,  $P_{H_2O}$ ). Starting phenocryst content was 5 vol.%.  $P_f$  was set to 10–40 MPa. All simulations were run at  $T = 950$ – $1050^\circ\text{C}$ ;  $T_i$  and  $T_f$  were allowed to vary independently. We used average  $dP/dt$  of  $1$ – $1000 \text{ MPa h}^{-1}$  ( $0.0003$ – $0.3 \text{ MPa s}^{-1}$ ). 40% of runs were linear decompressions, 30% accelerating, and 30% were two-step decompressions, whereby there was a pause following initial linear decompression and subsequent post-pause decompression was either linear or accelerating. A subset of experiments was declared to “fragment” at a pressure  $P_{frag}$  of 20–80 MPa during the simulations; these runs had  $dP/dt$  of  $1$ – $20 \text{ MPa h}^{-1}$  prior to fragmentation and increased to  $30$ – $400 \text{ MPa h}^{-1}$  following fragmentation. Runs that fragmented experienced cooling  $\Delta T_{frag}$  of up to  $60^\circ\text{C}$ , the upper bound suggested by Mastin and Ghiorso (2001) for adiabatic cooling of an erupting mixture of gas and ash.

**Table 3** Parameters used for SNGPlag modeling for the Curacautín magma

Parameter	Symbol	Values	Units
Initial pressure	$P_i$	110–150	MPa
Final pressure	$P_f$	10–50	MPa
Starting temperature	$T = T_i = T_f$	950–1050	$^\circ\text{C}$
Final temperature	$T = T_i = T_f$	950–1050	$^\circ\text{C}$
Decompression rate	$dP/dt$	5–250	$\text{MPa h}^{-1}$
Pause depth	$P_p$	40–120	MPa
Pause duration	$t$	0.1–10	hr
Pre-pause decompression	$dP/dt_{pre}$	5–100	$\text{MPa h}^{-1}$
Post-pause decompression	$dP/dt_{post}$	50–750	$\text{MPa h}^{-1}$
Fragmentation level	$P_{frag}$	20–60	MPa
Phenocryst content		5	vol.%

## Comparison of natural and modeled CSDs

Cumulative CSDs of natural samples describe the number of plagioclase crystals that are larger than each size bin. Using counting statistics, we can convert that size relationship into an uncertainty bound ( $\sigma_{\text{CSD}}$ ) at each size,  $\sigma_{\text{CSD}} = \sqrt{n_{\text{bin}}}$ , where  $n_{\text{bin}}$  is the number of microlite counts per size bin. The upper and lower bounds then define an envelope for natural CSDs (Fig. 3). Therefore, with higher  $n_{\text{bin}}$ , our uncertainty becomes smaller. Our modeled CSDs therefore have an effective uncertainty of zero as the billions of crystals compose each bin. This is not to say the modeling here is perfect, but rather that uncertainty is orders of magnitude greater in measurements of the natural samples.

## Modeling limitations

The experiments of Shea and Hammer (2013) were mostly quenched at higher pressures, with only two experiments decompressed to  $P_f$  of 22 and 10 MPa and  $\Delta T > 113^\circ\text{C}$  (Table 1). Those two experiments produced the highest plagioclase crystallinities of 34.8% and 46.1%, respectively. No experiments have been conducted at conditions where the melt viscosity should be highest. As such, our  $N_{\text{plag}}$  and  $G_{\text{plag}}$  for very high  $\Delta\phi_{\text{plag}}$  are extrapolated, although we note that any decompression path other than single-step will have some crystallization prior to reaching lower  $P$ , and therefore have a lower  $\Delta\phi_{\text{plag}}$  than a single step run initially has at

the same pressure. SNGPlag does not consider any unique conduit geometries or eruption style (e.g., dike geometry, ring faulting during eruption) that may impact late decompression or ascent dynamics. Shearing along conduit margins is not considered in SNGPlag but has been shown to impact crystallization (Vetere et al. 2021). Nucleation delay inversely correlates with  $\Delta T$  and may suppress crystallization up to  $\sim 100^\circ\text{C}$  at low  $\Delta T$  (Rusiecka et al. 2020), which could impact CSDs. SNGPlag does not explicitly consider nucleation delay in the crystallization calculations, but low growth rates acting upon small numbers will result in very low numbers of detectable crystals at early times or low  $\Delta T$ . Finally, the only volatile species considered in our modeling is  $\text{H}_2\text{O}$ , although the presence of  $\text{CO}_2$  or another volatile species should only affect the crystallization of plagioclase insofar as it reduces the partial pressure of  $\text{H}_2\text{O}$ .

## Results

### Instantaneous nucleation and growth rates of plagioclase

Instantaneous  $N_{\text{plag}}$  and  $G_{\text{plag}}$  curves have similar geometries (Fig. 4). The maximum  $N_{\text{plag}}$  of  $6.1 \times 10^5 \text{ cm}^{-3} \text{ h}^{-1}$  is reached at  $\Delta\phi_{\text{plag}} = 44 \text{ vol.}\%$ . The maximum  $G_{\text{plag}}$  of  $27.4 \mu\text{m h}^{-1}$  is reached at  $\Delta\phi_{\text{plag}} = 29 \text{ vol.}\%$ . There is very little  $N_{\text{plag}}$  activity at  $\Delta\phi_{\text{plag}} < 10\%$ , but the  $G_{\text{plag}}$  of these early crystals is quite high.  $N_{\text{plag}}$  and  $G_{\text{plag}}$  beyond maximum  $\Delta\phi_{\text{plag}}$  are extrapolated and may not be representative of nature.

### Model results

The large parameter space over which we modeled the Curaçutín eruption includes many runs that are physically unrealistic; we applied filters to remove those results. Our filters identified runs that begin and/or end  $> 10^\circ\text{C}$  above the plagioclase liquidus and removes them. This reduced the number of model runs from 100,000 to 13,283 (Table 4). Because our decompression rates vary in an exponential fashion, it is not appropriate to compare them in linear space, so we report our average decompression rates as  $\log_2$  values. For example, three decompression rates of 1, 9, and  $80 \text{ MPa h}^{-1}$  would yield a linear average rate of  $30 \text{ MPa h}^{-1}$ , but a more representative average rate is obtained in log space and yields  $9 \text{ MPa h}^{-1}$ .

Average Unit 1  $dP/dt$  are  $53\text{--}93 \text{ MPa h}^{-1}$  for L1,  $46\text{--}89 \text{ MPa h}^{-1}$  for L4, and  $87\text{--}95 \text{ MPa h}^{-1}$  for L6 (Figs. 5, 6). Average Unit 2  $dP/dt$  are  $62\text{--}93 \text{ MPa h}^{-1}$  (L8). Average Unit 3  $dP/dt$  are the slowest at  $6\text{--}55 \text{ MPa h}^{-1}$  (L10). Conversely, average Unit 4  $dP/dt$  are the fastest at  $104\text{--}141 \text{ MPa h}^{-1}$  (L18, Table 4). Unit 1 average durations of decompression  $t_{\text{avg}}$  are between 1.40 and 4.08 h for L1,

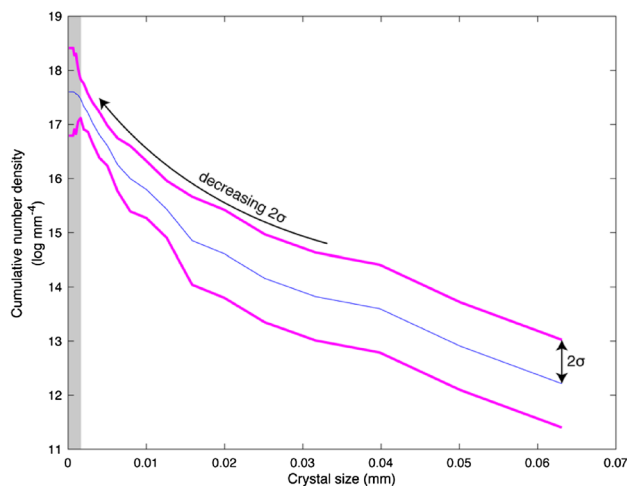


**Fig. 3** Example of how uncertainty is shown on our crystal size distribution (CSD) model runs (Supplemental Materials). The blue line is the natural cumulative CSD and the pink lines are the  $2\sigma$  error bounds calculated for each bin. Notice how  $2\sigma$  decreases with smaller microlite sizes. This is a result of the higher number of microlites counted in the natural samples at these size ranges. The increase in  $2\sigma$  near the y-intercept (gray field) results from a relative decrease in the number of smallest crystals counted in 2D measurements of the natural sample (Fig. 4) (Valdivia et al. 2022)



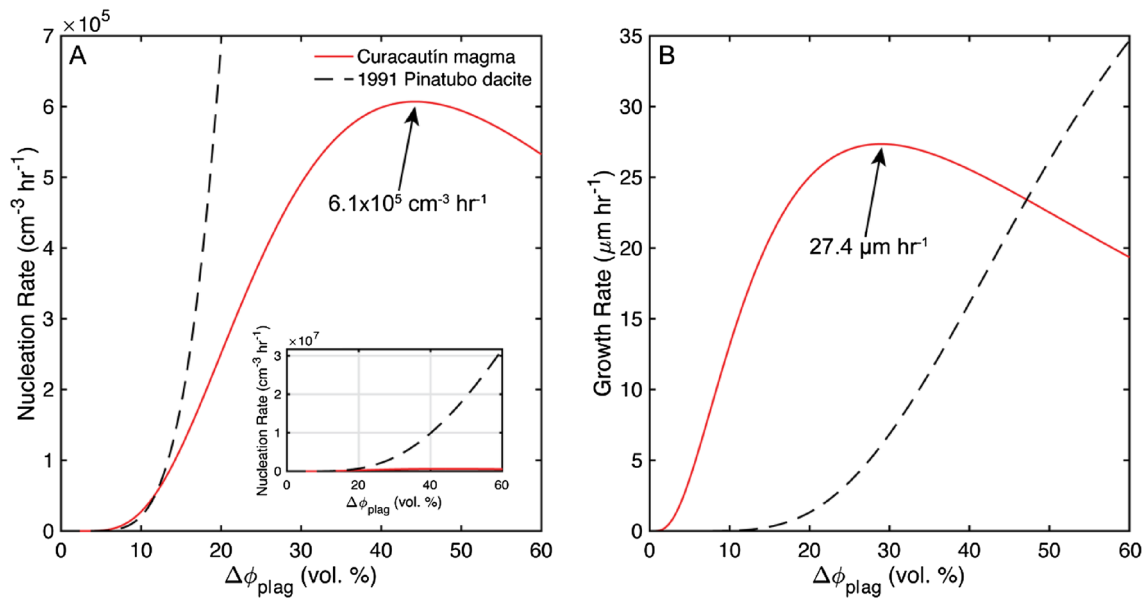


**Fig. 4** Modeled plagioclase nucleation (**A**) and growth (**B**) rate curves as a function of plagioclases supersaturation ( $\Delta\phi_{plag}$ ) for the 12.6 ka basaltic andesite Curacautín eruption and the 1991 Pinatubo dacite

2.40–4.69 h for L4, and 1.79–1.96 h for L6. Unit 2  $t_{avg}$  are between 1.69 and 2.02 h (L8). Unit 3  $t_{avg}$  are between 3.56 and 16.13 h (L10). Unit 4  $t_{avg}$  are between 0.87 and 0.96 h (L18, Figs. 5, 6, Table 4).

## Discussion

### Plagioclase nucleation and growth rates

$N_{plag}$  and  $G_{plag}$  curves (Fig. 4) for the basaltic andesite Curacautín magma have similar shapes, but very different magnitudes in comparison to those determined for the 1991 Pinatubo dacite (Befus and Andrews 2018). The Curacautín magma reaches a maximum  $N_{plag} = 6.1 \times 10^5 \text{ cm}^{-3} \text{ h}^{-1}$  at  $\Delta\phi_{plag} = 44 \text{ vol.}\%$  which is an order of magnitude lower than the Pinatubo dacite at the same  $\Delta\phi_{plag}$  (Fig. 4A). Conversely, the maximum Curacautín  $G_{plag}$  of  $27.4 \text{ } \mu\text{m h}^{-1}$  is reached at  $\Delta\phi_{plag} = 29 \text{ vol.}\%$ , whereas the 1991 Pinatubo  $G_{plag}$  for the same  $\Delta\phi_{plag}$  is  $6.0 \text{ } \mu\text{m h}^{-1}$  and does not reach  $27.4 \text{ } \mu\text{m h}^{-1}$  until  $\Delta\phi_{plag} \lesssim 52 \text{ vol.}\%$  (Fig. 4B). Indeed,  $G_{plag}$  is more than an order of magnitude higher in the mafic composition for  $\Delta\phi_{plag} \lesssim 5\%$ . Our modeled  $N_{plag}$  and  $G_{plag}$  suggest that although plagioclase nucleates more than an order of magnitude slower in basaltic andesites than in dacites at similar  $\Delta\phi_{plag}$  the growth rate  $G_{plag}$  in the mafic composition is generally an order of magnitude faster. Significantly, the difference in volumetric growth rate is  $\sim 1000$  times greater in the basaltic andesite (the linear growth rate  $G_{plag}$  raised to the third power). That is, a smaller number of crystals are able

to more rapidly grow and thus reduce  $\Delta\phi_{plag}$  in the mafic magma as compared to more silicic magmas. This explains the predominance of acicular plagioclase microlites commonly observed in the pyroclasts of mafic explosive eruptions (Constantini et al. 2010; Arzilli et al. 2019; Bamber et al. 2020; Rowe et al. 2021; Marshall et al. 2022a).

### Decompression rates

Natural plagioclase CSDs for the Ci are concave upward at the finest size bins (Valdivia et al. 2022). Valdivia et al. (2022) divided Ci CSDs into two segments based on linear regression fitting. Using experimentally derived growth rates of  $10^{-4} \text{ mm s}^{-1}$  (Arzilli et al. 2019),  $2 \times 10^{-5} \text{ mm s}^{-1}$  (Arzilli et al. 2015),  $10^{-6} \text{ mm s}^{-1}$  (Shea and Hammer 2013), and  $10^{-7} \text{ mm s}^{-1}$  (Arzilli et al. 2015), they calculated time-scales of crystallization from 2 s to 1.2 h for the smallest size fraction of plagioclase microlites in CSDs, and 8 s to 5.0 h for the largest size fraction. Here, we use cumulative natural CSDs for fitting to our modeled CSDs to remove downturns at the smallest size fractions observed by Valdivia et al. (2022).

Using the 1% population of isolated Ci vesicles, Valdivia et al. (2022) calculated average  $dP/dt$  for the Ci magma of  $0.84\text{--}1.95 \text{ MPa s}^{-1}$  for Unit 1,  $0.36 \text{ MPa s}^{-1}$  for Unit 2,  $2.60 \text{ MPa s}^{-1}$  for Unit 3, and  $0.55 \text{ MPa s}^{-1}$  for Unit 4 using the BND meter of Toramaru (2006), with a minimum average  $dP/dt$  for the Curacautín eruption of  $1.4 \text{ MPa s}^{-1}$ . Our average modeled  $dP/dt$  rates ( $0.18 \times 10^{-2}\text{--}3.9 \times 10^{-2} \text{ MPa s}^{-1}$ ) are approximately two orders of magnitude slower

**Table 4** Summary of 150,000 SNGPlag results. Three natural crystal size distributions (CSDs) for each sample were modeled. For each model run, SNGPlag generates a series of fits to the natural CSDs, denoted below as CSD fit. Fit f1 corresponds to the model runs that best fit the natural CSDs bins within  $2\sigma$  (out of 31 total bins). Fit f2 is the second best fit and is determined by removing one bin from the total bins that fit. Fit f3 removes one additional bin

Sample	L1	L4			L6			L8			L10			L18		
Unit	1							2			3			4		
Runs with $P_i = 110\text{--}150$ MPa and $P_j = 10\text{--}50$ MPa (n=100,000)																
CSD fit	f1	f2	f3	f1	f2	f3	f1	f2	f3	f1	f2	f3	f1	f2	f3	f1
CSD	18/31	17/31	16/31	17/31	16/31	15/31	21/31	20/31	19/31	21/31	20/31	19/31	15/31	14/31	13/31	20/31
bins																
n	21	155	850	92	1297	7072	23	69	128	4	42	108	2	7	3364	2
$\text{Log}_2$	6.31	6.11	5.09	5.93	5.09	4.90	6.06	6.15	6.09	5.82	6.01	6.08	2.69	3.55	5.29	6.69
$dP/$	(0.90)	(1.18)	(1.37)	(1.38)	(1.37)	(1.33)	(1.08)	(1.22)	(1.23)	(0.74)	(1.17)	(1.26)	(0.09)	(1.45)	(1.25)	(0.10)
$dt_{avg}$																
( $1\sigma$ )																
(MPa																
$\text{h}^{-1}$ )																
Median	90	77	32	65	35	29	64	80	77	59	65	81	6	7	41	104
$dP/dt$																
(MPa																
$\text{h}^{-1}$ )																
Range	20–185	8–243	5–250	7–250	5–250	5–250	14–229	11–229	11–231	29–100	11–231	11–231	6–7	6–53	5–250	99–109
of																
$dP/dt$																
(MPa																
$\text{h}^{-1}$ )																
$t_{avg}$ ( $1\sigma$ )	1.40	1.88	4.08	2.40	4.26	4.69	1.79	1.92	1.96	1.69	1.95	2.02	16.13	11.22	3.56	0.87
(hr)	(0.98)	(1.78)	(3.45)	(2.62)	(4.04)	(3.99)	(1.49)	(1.94)	(1.91)	(0.68)	(1.82)	(1.99)	(0.29)	(6.65)	(3.51)	(0.25)
$P_{f_{avg}}$	120.95	120.82	123.85	121.32	125.27	125.38	119.02	119.00	119.24	126.80	120.31	119.76	130.38	124.52	125.11	118.46
( $1\sigma$ )	(7.24)	(7.00)	(9.34)	(7.52)	(9.66)	(10.18)	(5.88)	(5.32)	(5.80)	(9.95)	(6.90)	(6.10)	(13.34)	(9.41)	(10.36)	(2.73)
(MPa)																
$P_{f_{avg}}$	27.89	27.79	28.47	28.07	28.43	28.44	27.46	27.42	27.47	36.22	29.39	28.88	25.77	28.31	29.41	28.99
( $1\sigma$ )	(10.44)	(11.28)	(11.38)	(11.00)	(11.39)	(11.46)	(12.49)	(12.68)	(12.02)	(13.04)	(11.82)	(12.02)	(21.86)	(11.92)	(11.64)	(22.33)
(MPa)																
Runs with $P_i = 15\text{--}30$ MPa and $P_j = 3\text{--}10$ MPa (n=50,000)																
CSD fit	f1	f2	f3	f1	f2	f3	f1	f2	f3	f1	f2	f3	f1	f2	f3	f1
CSD	18/31	17/31	16/31	17/31	16/31	15/31	21/31	20/31	19/31	20/31	19/31	18/31	14/31	13/31	12/31	20/31
bins																
n	19	188	586	51	1252	6665	29	82	155	55	168	291	4	8607	19,364	22
$\text{Log}_2$	4.20	5.24	4.73	4.53	4.49	4.33	4.94	5.08	5.34	5.57	5.51	5.46	2.86	5.08	5.20	6.00
$dP/$	(1.02)	(1.42)	(1.64)	(1.25)	(1.68)	(1.58)	(1.29)	(1.45)	(1.46)	(1.47)	(1.40)	(1.39)	(0.49)	(1.64)	(1.53)	(0.86)
$dt_{avg}$																
( $1\sigma$ )																
(MPa																
$\text{h}^{-1}$ )																
Median	19	37	24	24	16	14	26	33	37	49	48	47	7	31	38	68
$dP/dt$																
(MPa																
$\text{h}^{-1}$ )																
Range	14–244	50–206	99–109	41	104	110	151									



Table 4 (continued)

Sample	L1	L4	L6	L8	L10	L18	
Unit	1			2	3	4	
Range of $dP/dt$ (MPa h <sup>-1</sup> )	6–94	5–246	5–316	5–242	5–247	5–344	6–245
$t_{\text{avg}}$ (1 $\sigma$ ) (hr)	1.09 (0.64)	1.17 (1.15)	1.33 (1.06)	0.71 (0.76)	0.59 (0.68)	0.73 (0.80)	0.42 (0.49)
$P_{i,\text{avg}}$ (1 $\sigma$ ) (MPa)	23.02 (3.45)	23.91 (4.05)	23.37 (4.27)	22.98 (3.93)	22.83 (4.03)	22.25 (4.44)	22.88 (4.23)
$P_{f,\text{avg}}$ (1 $\sigma$ ) (MPa)	6.06 (1.98)	6.35 (2.00)	6.35 (2.01)	6.23 (2.10)	6.47 (2.02)	6.49 (2.02)	6.67 (1.97)

than the rates calculated by Valdivia et al. (2022, Fig. 7, Table 4). The bubble textures investigated by Valdivia et al. (2022) represent two distinct phases of Curacautín magma evolution. The highly tortuous vesicle network of > 99% pore volume is indicative of relatively slow ascent (e.g., Marshall et al. 2022b), whereas the small, isolated vesicles likely formed during an episode of homogeneous nucleation very late in ascent or syn-eruptively at low pressures in the shallow subsurface (Mangan and Sisson 2000) where  $dP/dt$  are greatest. Conversely, our average  $dP/dt$  modeled with SNGPlag represent pressures from 10 to 150 MPa where rates of decompression begin slow and increase over time (Supplemental Material). Together, our work and that of Valdivia et al. (2022), suggests that decompression (and therefore ascent) rates increase by orders of magnitude at the shallowest conduit depths (Fig. 7) or during fragmentation. Interestingly, the decompression rates modeled here are in agreement with those modeled by La Spina et al. (2021) for highly explosive eruptions, and the decompression rates calculated by Valdivia et al. (2022) are consistent with rates associated with high fountaining (La Spina et al. 2021) and may further support the boiling over eruption model proposed in Marshall et al. (2022a).

The low water content of the Ci melt ( $1.1 \pm 0.32\%$ ; Schindlbeck et al. 2014) suggests storage at shallower depths, or water undersaturation. We conducted a second, smaller set of experiments ( $n=50,000$ ) at  $P_i=15\text{--}30$  MPa and  $P_f=3\text{--}10$  MPa to investigate crystallization over a shorter decompression window from shallower depths (Table 4). Average  $dP/dt$  for Unit 1 are  $24\text{--}59$  MPa h<sup>-1</sup> (L1),  $34\text{--}46$  MPa h<sup>-1</sup> (L4), and  $46\text{--}61$  MPa h<sup>-1</sup> (L6). Unit 2  $dP/dt$  are  $66\text{--}75$  MPa h<sup>-1</sup>. Unit 3 average  $dP/dt$  are  $8\text{--}61$  MPa h<sup>-1</sup>. Finally, average Unit 4  $dP/dt$  are  $74\text{--}80$  MPa h<sup>-1</sup>. These rates tend to be slower than those modeled for deeper chamber conditions but are generally within the same order of magnitude (Table 4). Because Schindlbeck et al. (2014) estimated a chamber depth of ~ 18 km for the Curacautín magma, the  $dP/dt$  calculated with  $P_i$  up to 150 MPa are likely a more reasonable approximation of Curacautín decompression (Fig. 7).

The  $dP/dt$  modeled here for the Curacautín magma are similar to  $dP/dt$  calculated or estimated for other mafic eruptions using decompression experiments and diffusion modeling, but are orders of magnitude lower than mafic  $dP/dt$  calculated from bubble textures (Fig. 8). Homogeneous bubble nucleation events create densely packed networks of bubbles at very shallow depths where rates of  $dP/dt$  are highest (Mangan and Sisson 2000), and thus  $dP/dt$  determined from bubble textures may only reflect very shallow ascent conditions and not be representative of conditions from deeper in the conduit. Conversely, our modeling here reflects ascent rates integrated over the entire conduit and not just the shallowest depths and likely records more of the

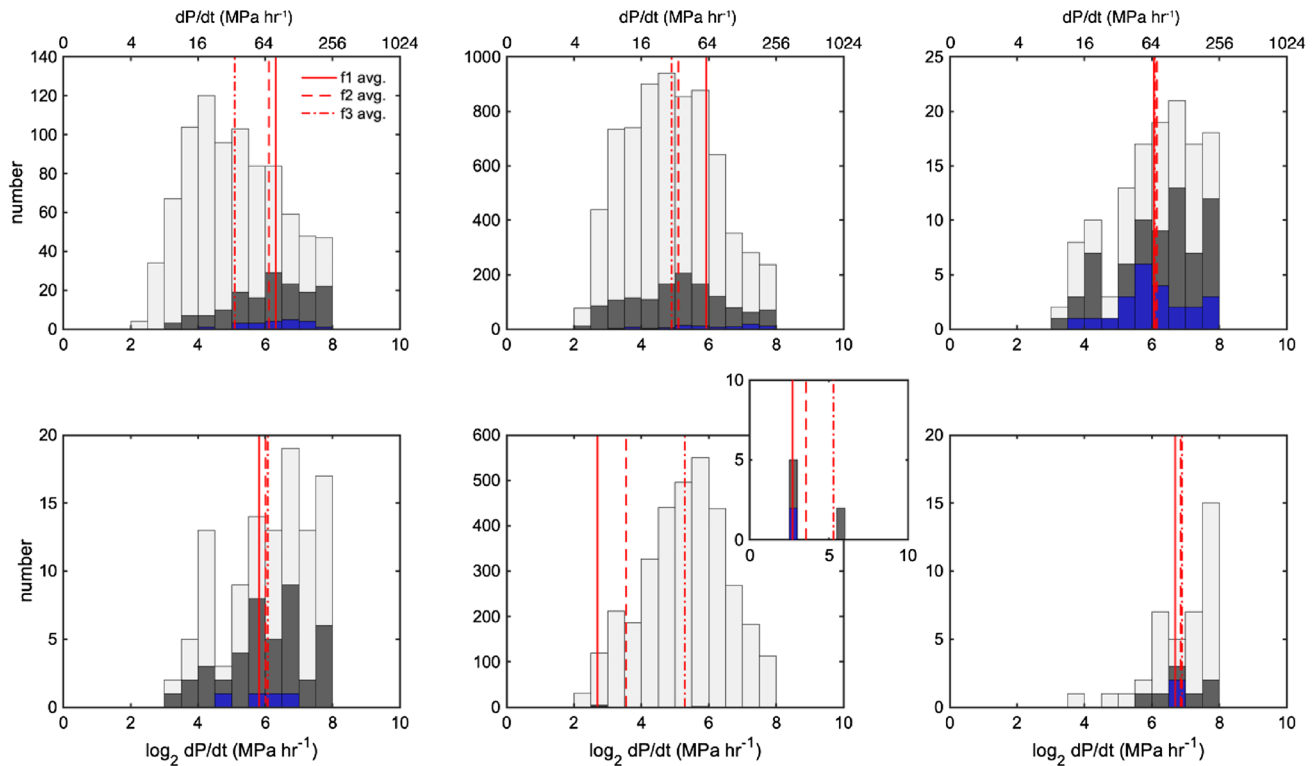


**Fig. 5** Histograms of  $C_i$  decomposition rates plotted in linear space (top y-axis) and  $\log_2$  space (bottom y axis) modeled using SNGPlag. Blue bars are f1 fits, dark gray are f2 fits, and light gray are f3 fits (see description in body text). Averages are shown as red lines. **A** L1. **B** L4. **C** L3. **D** L8. **E** L10. Inset is zoomed in to f1 and f2 fits. Inset axes units are the same as the large plots. **F** L18

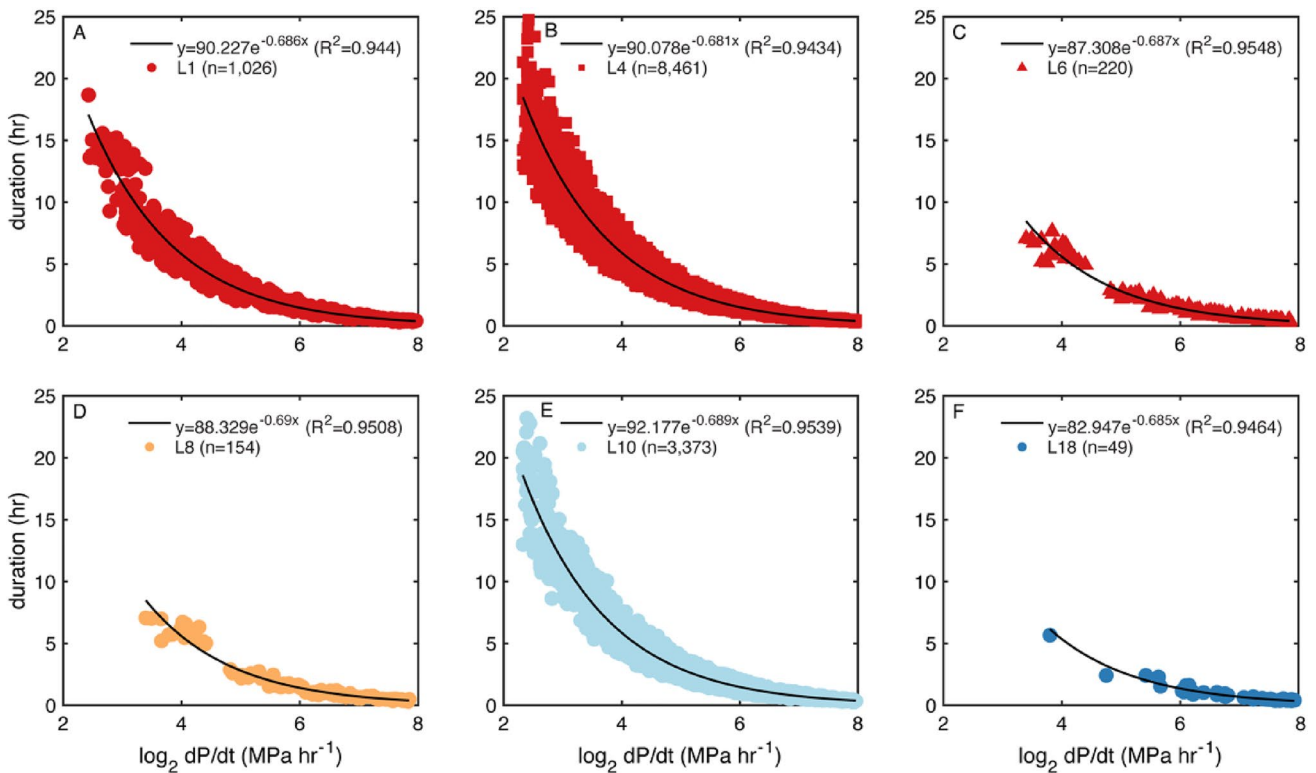


**Fig. 6** Plots of filtered  $\log_2 dP/dt$  ( $\text{MPa h.}^{-1}$ ) versus duration of decompression (h). **A** L1, Unit 1. **B** L4, Unit 1. **C** L6, Unit 1. **D** L8, Unit 2. **E** L10, Unit 3. **F** L18, Unit 4

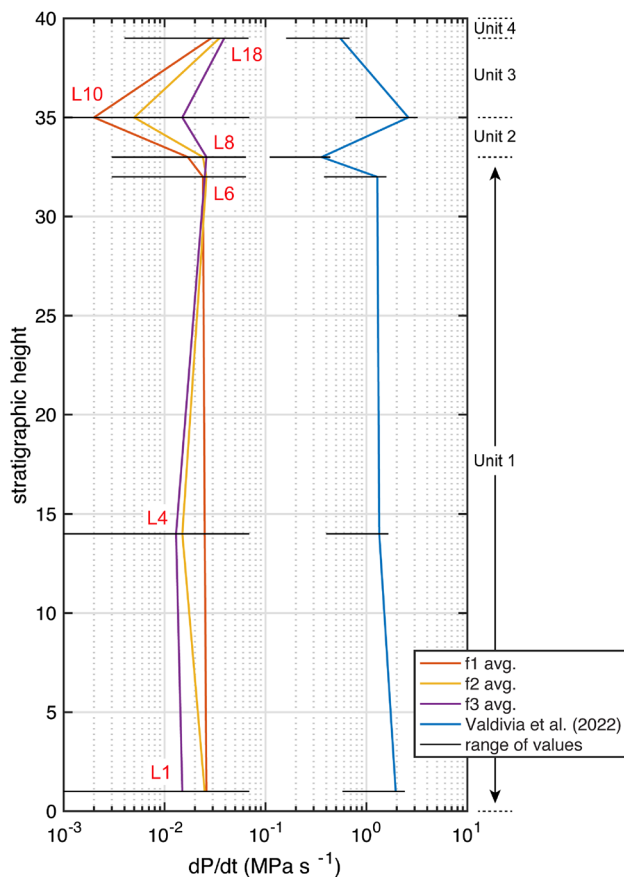


**Fig. 7** Curacautín ignimbrite (Ci) decompression rates ( $dP/dt$ ) modeled using SNGPlag plotted with respect to Ci stratigraphy (m) (Marshall et al. 2022a) along with the  $dP/dt$  calculated by Valdivia et al. (2022) from x-ray computed microtomography 3D renderings and using the bubble number density rate meter of Toramaru (2006). Sample names are provided in red and associated units are plotted along the right y-axis. SNGPlag curves are provided for all three crystal size distribution fits (see explanation in Table 3).  $dP/dt$  results plotted are those from the 100,000 model run dataset (Table 4)

decompression history, albeit perhaps not the final, shallowest portions.

### Magma ascent rates

Decompression rates do not have the same relationship to ascent rate at all volcanoes. This results from differences in lithostatic or magmatic pressure gradients at different volcanoes, which is impacted by factors such as crustal thickness, country rock compositions and densities, conduit geometry, and elevation. In addition, particular decompression speedometers may be sensitive to the partial pressure of a particular volatile species, not total pressure ( $P_{total}$ ); SNGPlag is sensitive to  $P_{H_2O}$ , which is less than  $P_{total}$  when the system is water undersaturated or saturated with a mixed volatile phase. Here, we consider

two simplified scenarios to derive first order estimates of magma ascent rate from our modeled decompression rates, and then compare those rates with a calculated lithostatic pressure gradient ( $dP/dz$ ) for the crust beneath Llaima.

Our first estimate assumes that  $P_{H_2O} = P_{total}$  and that there is no other volatile species in our system. This of course is an oversimplification as there would be some amount of  $P_{CO_2}$  present as well as others volatile species in minor concentrations. If we also assume that a  $dP/dz = 90$  MPa per every 4 km is reasonable for a mix of mafic lavas and granitic plutons (Naranjo and Moreno 2005), then we obtain average Unit 1 ascent rates for the Ci of  $0.66 \pm 0.67$ – $1.13 \pm 0.78$  m s<sup>-1</sup> for L1,  $0.66 \pm 0.58$ – $1.10 \pm 0.86$  m s<sup>-1</sup> for L4, and  $1.07 \pm 0.80$ – $1.17 \pm 0.80$  m s<sup>-1</sup> for L6. Our Unit 2 (L8) average ascent rates are  $0.77 \pm 0.37$ – $1.14 \pm 0.81$  m s<sup>-1</sup>. Unit 3 (L10) average ascent rates are the slowest at  $0.08 \pm 0.01$ – $0.68 \pm 0.58$  m s<sup>-1</sup>. Conversely, Unit 4 (L18) average ascent rates are the fastest at  $1.28 \pm 0.09$ – $1.74 \pm 0.84$  m s<sup>-1</sup>. Due to our assumptions and simplifications, these rates should be considered a minimum (Fig. 9).

Our second calculation combines our modeling parameter space with a chamber depth estimate of 18 km (Schindlbeck et al. 2014). If we assume the Ci magma is water undersaturated, then we can expect the magma resided at a greater depth prior to decompression. Using a maximum  $P_i$  during SNGPlag modeling of 120 MPa, we obtain an effective  $dP/dz$  in  $P_{H_2O}$  of 60 MPa per every 9 km. Using these new assumptions, our ascent rates for the Ci magma increase. Average ascent rates for Unit 1 become  $2.23 \pm 2.27$ – $3.89 \pm 2.04$  m s<sup>-1</sup> (L1),  $1.90 \pm 1.97$ – $3.72 \pm 2.90$  m s<sup>-1</sup> (L4), and  $3.61 \pm 2.68$ – $3.96 \pm 2.71$  m s<sup>-1</sup> (L6). Unit 2 average ascent rates are  $2.58 \pm 1.24$ – $3.86 \pm 2.73$  m s<sup>-1</sup>. Unit 3 average ascent rates are  $0.27 \pm 0.02$ – $2.30 \pm 1.97$  m s<sup>-1</sup>. Finally, Unit 4 average ascent rates are  $4.31 \pm 0.30$ – $5.86 \pm 2.85$  m s<sup>-1</sup>. Because this second set of ascent rates assumes the same decompression rates as our first scenario but over a greater depth, they should be considered maximum estimates (Fig. 9).

Finally, Schindlbeck et al. (2014) report a  $dP/dz$  at Llaima of  $\sim 20$  MPa km<sup>-1</sup> down to the brittle-ductile transition located at  $\sim 14$ – $15$  km. Using their  $dP/dz$ , we calculated ascent rates for Unit 1 of  $0.63 \pm 0.66$ – $1.32 \pm 0.90$  m s<sup>-1</sup>,  $0.86 \pm 0.41$ – $1.29 \pm 0.91$  m s<sup>-1</sup> for Unit 2,  $0.09 \pm 0.01$ – $0.77 \pm 0.66$  m s<sup>-1</sup> for Unit 3, and  $1.44 \pm 0.10$ – $1.95 \pm 0.95$  m s<sup>-1</sup> for Unit 4 (Fig. 7). These rates are closer to our lower end approximation. Note that Schindlbeck et al. (2014) estimated a storage depth of 18 km for the Curacautín magma, and thus their  $dP/dz$  may be a minimum.

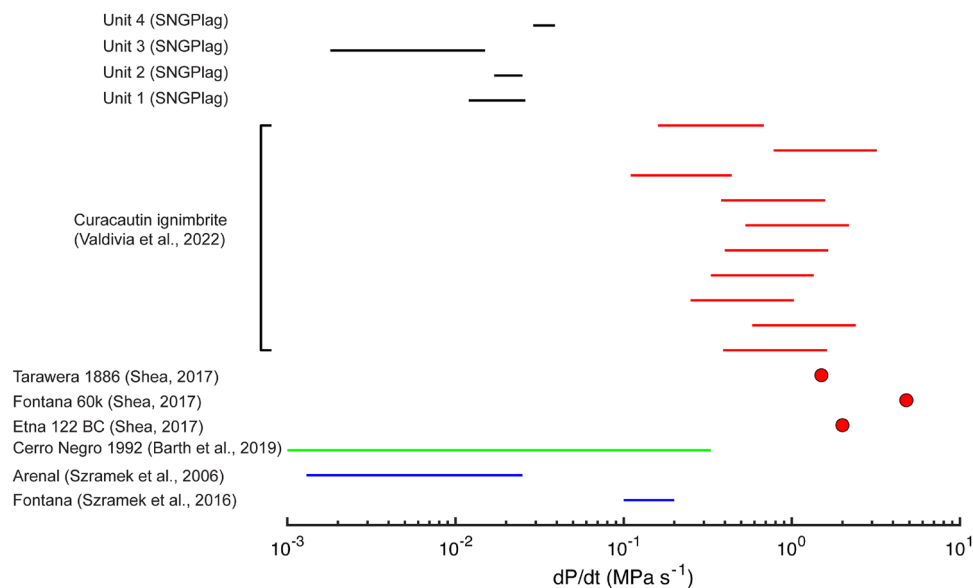
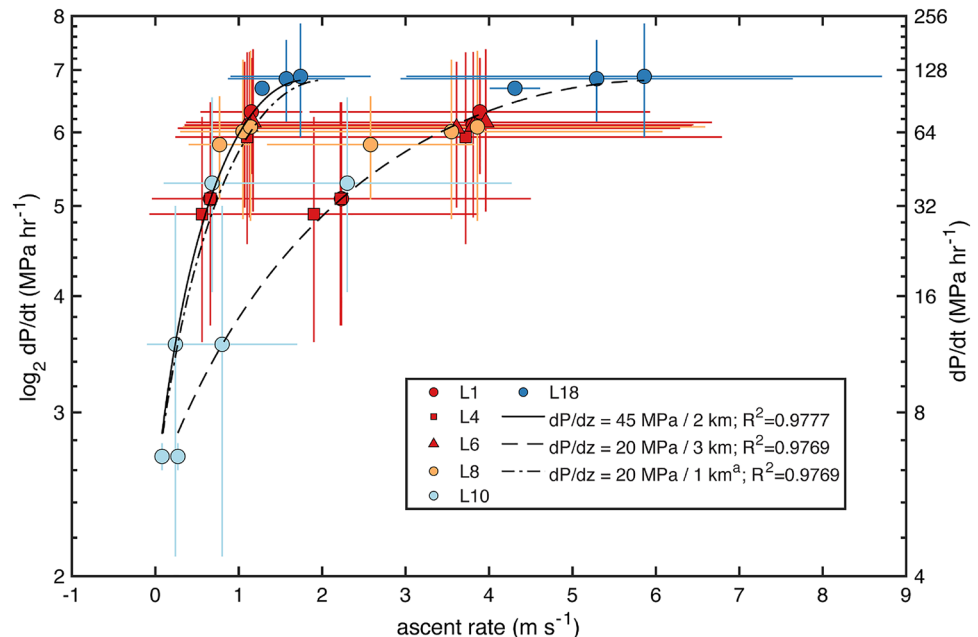


**Fig. 8** The range of decompression rates ( $dP/dt$ ) for mafic magmas estimated using different methods. Blue = decompression experiments. Green = diffusion modeling. Red = bubble number density (BND). Black = SNGPlag. SNGPlag modeling has the most overlap with decompression experiments and diffusion modeling. The similarity of our modeled  $dP/dt$  to decompression experiments is likely

due to the way SNGPlag is calibrated using Shea and Hammer (2013) data.  $dP/dt$  calculated using BND data are consistently orders of magnitude higher. This may be a function of using bubbles from homogeneous nucleation events which occur at very shallow depths and reflect moments of very high  $dP/dt$  (Mangan and Sisson 2000)

**Fig. 9** Curacautín magma ascent rates ( $m s^{-1}$ ) versus decompression rate in both  $\log_2 dP/dt$  and  $dP/dt$  ( $MPa h^{-1}$ ). Polynomial fits to our minimum and maximum end-member estimates for lithostatic pressure gradient ( $dP/dz$ ) and that of Schindlbeck et al. (2014) are provided. Points for Schindlbeck et al. (2014) curve are not plotted. Bars are  $1\sigma$ . Colors correspond with those in Fig. 6



### Difficulty of fitting smallest CSD microlites

SNGPlag struggles to fit the smallest crystal sizes in the observed plagioclase CSDs. This may be a result of the tighter  $2\sigma$  bounds at smaller sizes because the number of crystals exceeding those sizes is large, therefore decreasing the uncertainty allowed in the model fits (Fig. 3).

Alternatively, poor fits at small microlite sizes may result from the range of  $P$  values reported in the experiments of Shea and Hammer (2013) that we used for calibration of SNGPlag  $N_{plag}$  and  $G_{plag}$  rates (Table 1). The lowest  $P_f$  used for calibration are 10 and 22 MPa, but these were only two out of the eleven experiments, whereas the other nine were conducted to  $42 \leq P_f \leq 100$  MPa (Shea and Hammer 2013).



Because  $N_{plag}$  and  $G_{plag}$  are not linear with respect to  $\Delta\phi_{plag}$  (Fig. 4), they should be higher in experiments conducted at very low  $P$ , corresponding to high  $\Delta\phi_{plag}$ , although this extrapolation does not account for much high viscosities potentially retarding the nucleation and growth rates. Our modeled  $P_f$  and calibration  $P_f$  stop at 10 MPa, but natural plagioclase textures likely continue to record shallower conduit conditions. In this scenario, we would expect crystallization of a higher number of smaller plagioclase microlites, which may have produced the densely crystalline Ci pyroclasts (Marshall et al. 2022a, b; Valdivia et al. 2022).

### Interpreting the Curacautín eruption

Rapid magma ascent rates are often invoked to explain mafic Plinian and ignimbrite-forming eruptions (Sable et al. 2006, 2009; Vinkler et al. 2012; Arzilli et al. 2019; Bamber et al. 2020; Marshall et al. 2022a; Valdivia et al. 2022). Super-saturation resulting from rapid ascent drives plagioclase nucleation and crystallization. Our modeling here reveals that  $N_{plag}$  in the basaltic andesite Ci is considerably lower than  $N_{plag}$  in dacites, but maximum  $G_{plag}$  of  $7.6 \times 10^{-7} \text{ cm s}^{-1}$  is volumetrically up to 1000× greater than dacite  $G_{plag}$  at the same  $\Delta\phi_{plag}$ . Our  $G_{plag}$  is one order of magnitude lower than the  $\sim 3\text{--}5 \times 10^{-6} \text{ cm s}^{-1}$  measured by Vetere et al. (2021) during basaltic andesite viscosity experiments. Those authors argue for the importance of shear rate being considered in models of magmatic and volcanic processes, which is not something considered in this version of SNGPlag (Table 2). Indeed, shear rate and its impact on viscosity would impact our  $G_{plag}$  and may help explain conduit processes proposed by Marshall et al. (2022b).

Our modeling here suggests that rapid  $dP/dt$  produced the plagioclase microlite textures observed in Ci pyroclasts (Table 3; Marshall et al. 2022a, b; Valdivia et al. 2022). Such extensive crystallization would have increased the magma viscosity to the point that vesicles would begin to distort and wrap around the nucleating and rapidly growing acicular plagioclase. This explains the highly tortuous 99% interconnectivity vesicle population textures identified by Valdivia et al. (2022). Highly tortuous vesicle networks inhibit outgassing, which in turn enhances the overpressure necessary for brittle fragmentation.

The three sets of magma ascent rates we estimated here using different  $dP/dz$  reasonable for the South Central Volcanic Zone of Chile offer a first-order look into the ascent rates that drove the Curacautín eruption (Fig. 9). Minimum ascent rates of  $0.1\text{--}1.7 \text{ m s}^{-1}$  using a  $dP/dz$  of  $22.5 \text{ MPa km}^{-1}$  are similar to the ascent rates of  $0.1\text{--}2.0 \text{ m s}^{-1}$  we estimated using the  $dP/dz$  of Schindlbeck et al. (2014). Conversely, a  $dP/dz$  of 20 MPa per every 3 km yields ascent rates up to 3× faster (Fig. 9).

Unit 1 ascent rates are variable between  $0.6$  and  $1.3 \text{ m s}^{-1}$  and increase slightly to  $0.8\text{--}1.3 \text{ m s}^{-1}$  in Unit 2. Unit 3 ascent rates drop by an order of magnitude to  $0.1\text{--}0.8 \text{ m s}^{-1}$  and suggests modulation of the magma flux during the Curacautín eruption. Unit 4 has the fastest magma ascent rate of  $1.3\text{--}2.0 \text{ m s}^{-1}$  and represents the final pulse of the Ci eruption. Valdivia et al. (2022) calculated vesicle overpressures necessary to fragment the Ci magma between 3.8 and 5.1 MPa. Such a low fragmentation threshold combined with the rapid  $dP/dt$  calculated here implies a limited decompression history prior to climatic fragmentation. Because the Ci was produced during a single eruptive event (Marshall et al. 2022a), changes in magma ascent rate did not likely result from changes in shallow magma storage or magma recharge, but rather changes in vesiculation or conduit/vent geometry during eruption. Discriminating between those different parameters is beyond the scope of the current version of SNGPlag.

The rapid  $G_{plag}$  calculated in our modeling would generate acicular plagioclase morphologies that produce highly tortuous vesicle networks that inhibit outgassing. Following fragmentation, decompression and ascent rates of the gas-pyroclast mixture are orders of magnitude greater than the original bulk magma and suggest there is little time between fragmentation and eruption. In the case of the Ci, the time period between fragmentation and eruption likely generated the highly crystalline groundmass of  $l < 10 \mu\text{m}$  plagioclase microlites that overprints sutures between fused domains of heterogeneous vesicle textures discussed in Marshall et al. (2022b). These results help elucidate the still poorly understood conduit processes that impact how mafic magmas can erupt as large, explosive events.

### Conclusions

Plagioclase nucleation and growth rates,  $N_{plag}$  and  $G_{plag}$ , respectively, differ substantially between mafic and felsic magmas. Those differences can affect eruption style. Modeled maximum  $N_{plag}$  for the 12.6 ka basaltic andesite Curacautín eruption are orders of magnitude lower than those for the 1991 Pinatubo dacite (Fig. 4);  $G_{plag}$ , however, is up to 10× greater in mafic magmas than felsic magmas, resulting in volumetric growth rates  $\sim 1000\times$  greater in mafic magmas than felsic ones. This result explains the predominately acicular nature of plagioclase microlites in the products of mafic explosive eruptions attributed to rapid ascent rates.

The  $dP/dt$  modeled here for the Ci eruption using SNGPlag are between  $10^{-3}$  and  $10^{-1} \text{ MPa s}^{-1}$  and are similar to  $dP/dt$  measured experimentally for similar compositions and known eruption styles (e.g., Arzilli et al. 2019; La Spina et al. 2021; Bamber et al. 2020). We were able to fit the majority of CSD bins to the natural samples. Unlike decompression experiments

which must follow some particular decompression pathway(s) (Fig. 1), our modeling applies instantaneous  $N_{plag}$  and  $G_{plag}$  to produce thousands of possible decompression pathways to derive the most likely decompression scenario, and thus reflect the total decompression path of the Ci magma. Our modeled  $dP/dt$  are  $\sim 2$  orders of magnitude lower than those calculated by Valdivia et al. (2022) for the same eruption. This difference reflects time-integrated rates recording most of magma decompression and ascent presented here, whereas those of Valdivia et al. (2022) were calculated using the BND meter of Toramaru (2006) on a homogenous nucleation event in the shallow conduit. Importantly, these two sets of  $dP/dt$  reveal that decompression (and therefore magma ascent) of the Curacautín magma increased by orders of magnitude following the onset of fragmentation and record the explosive nature of the eruption. In addition, such a dramatic change in ascent rate would have similar impacts on  $\Delta\phi_{plag}$  (Fig. 4), resulting in the crystallization of the  $l < 10\ \mu\text{m}$  population of unbroken plagioclase microlites identified by Marshall et al. (2022b) and may explain the rapid crystallization times Valdivia et al. (2022) calculated from plagioclase CSDs.

Future work is necessary to fully describe the effects of decompression on crystallization and eruption processes described here. Integrating a viscosity component into SNG-Plag would allow us to investigate viscosity's role on ascent dynamics, which has profound impacts on degassing and crystallization and may help explain the textures reported in Marshall et al. (2022b). Plagioclase is not the only crystal phase in many mafic eruptions, and future modeling should consider additional crystal phases such as pyroxenes and olivine in addition to plagioclase. Finally, future decompression experiments conducted to very low  $P_i$  (and therefore higher melt viscosity) would enhance the calibration parameter space of SNGPlag and allow for the investigation of crystallization at the shallowest depths of conduits where microlites are likely to crystallize most extensively.

**Supplementary Information** The online version contains supplementary material available at <https://doi.org/10.1007/s00410-023-02030-y>.

**Acknowledgements** This work was supported by National Science Foundation EAR grant 1831143 and a Smithsonian Institution Pre-Doctoral Fellowship awarded to AM. The authors would like to thank Mike Ramshaw for his assistance with parallelizing SNGPlag. The content of this manuscript was improved by thoughtful comments from Fabio Arzilli and an anonymous reviewer. We'd also like to thank editor Mark Ghiorso for his handling of the manuscript during peer review.

**Data availability** Data is available upon request from the authors.

## Declarations

**Conflict of interest** The authors declare no competing interests.

**Open Access** This article is licensed under a Creative Commons Attribution 4.0 International License, which permits use, sharing, adaptation, distribution and reproduction in any medium or format, as long

as you give appropriate credit to the original author(s) and the source, provide a link to the Creative Commons licence, and indicate if changes were made. The images or other third party material in this article are included in the article's Creative Commons licence, unless indicated otherwise in a credit line to the material. If material is not included in the article's Creative Commons licence and your intended use is not permitted by statutory regulation or exceeds the permitted use, you will need to obtain permission directly from the copyright holder. To view a copy of this licence, visit <http://creativecommons.org/licenses/by/4.0/>.

## References

- Andrews BJ, Befus KS (2020) Supersaturation Nucleation and Growth of Plagioclase: a numerical model of decompression-induced crystallization. *Contrib Miner Petrol* 175:23. <https://doi.org/10.1007/s00410-020-1660-9>
- Andrews BJ, Gardner JE (2010) Effects of caldera collapse on conduit dimensions and magma decompression rate: an example from the 1800  $^{14}\text{C}$  yr BP eruption of Ksudach Volcano, Kamchatka, Russia. *J Volcanol Geotherm Res* 198:205–216. <https://doi.org/10.1016/j.jvolgeores.2010.08.021>
- Arzilli F, Agostini C, Landi P, Fortunati A, Mancini L, Carroll M (2015) Plagioclase nucleation and growth kinetics in a hydrous basaltic melt by decompression experiments. *Contrib Miner Petrol* 170:55. <https://doi.org/10.1007/s00410-015-1205-9>
- Arzilli F, La Spina G, Burton MR, Polacci M, Le Gall N, Hartley ME, Di Genova D, Cai B, Vo NT, Bamber EC, Nonni S, Atwood R, Llewellyn EW, Brooker RA, Mader HM, Lee PD (2019) Magma fragmentation in highly explosive basaltic eruptions induced by rapid crystallization. *Nat Geosci* 12:1023–1028. <https://doi.org/10.1038/s41561-019-0468-6>
- Bamber EC, Arzilli F, Polacci M, Hartley ME, Fellowes J, Di Genova D, Chavarría D, Saballos JA, Burton MR (2020) Pre- and syn-eruptive conditions of a basaltic Plinian eruption at Masaya Volcano, Nicaragua: the Masaya Triple Layer (2.1 ka). *J Volcanol Geotherm Res* 392:106761. <https://doi.org/10.1016/j.jvolgeores.2019.106761>
- Barth A, Newcombe M, Plank T, Gonnermann H, Hajimirza S, Soto GJ, Saballos A, Hauri E (2019) Magma decompression rate correlates with explosivity at basaltic volcanoes—constraints from water diffusion in olivine. *J Volcanol Geotherm Res* 387:106664. <https://doi.org/10.1016/j.jvolgeores.2019.106664>
- Befus KS, Andrews BJ (2018) Crystal nucleation and growth produced by continuous decompression of Pinatubo magma. *Contrib Miner Petrol* 173:92. <https://doi.org/10.1007/s00410-018-1519-5>
- Blundy J, Cashman KV (2008) Petrologic reconstruction of magmatic system variables and processes. *Rev Miner Geochem* 69(1):179–239. <https://doi.org/10.2138/rmg.2008.69.6> (In: Putirka KD, Tepley III FJ (eds) *Minerals, inclusions and volcanic processes*)
- Browne B, Gardner JE (2006) The influence of magma ascent path on the texture, mineralogy, and formation of hornblende reaction rims. *Earth Planet Sci Lett* 246:161–176. <https://doi.org/10.1016/j.epsl.2006.05.006>
- Brugger CR, Hammer JE (2010) Crystal size distribution analysis of plagioclase in experimentally decompressed hydrous rhyodacite magma. *Earth Planet Sci Lett* 300(3):246–254. <https://doi.org/10.1016/j.epsl.2010.09.046>
- Burgisser A, Gardner JE (2005) Experimental constraints on degassing and permeability in volcanic conduit flow. *Bull Volcanol* 67:42–56. <https://doi.org/10.1007/s00445-004-0359-5>
- Cashman KV, Marsh BD (1988) Crystal size distribution (CSD) in rocks and the kinetics and dynamics of crystallization II.

- Makaopuhi Lava Lake. *Contrib Miner Petrol* 99:292–305. <https://doi.org/10.1007/BF00375363>
- Castro JM, Dingwell DB (2009) Rapid ascent of rhyolitic magma at Chaitén volcano, Chile. *Nature* 461:780–783. <https://doi.org/10.1038/nature08458>
- Constantini L, Houghton BF, Bonadonna C (2010) Constraints on eruption dynamics of basaltic explosive activity derived from chemical and microtextural study: the example of the Fontana Lapilli Plinian eruption, Nicaragua. *J Volcanol Geotherm Res* 189:207–224. <https://doi.org/10.1016/j.jvolgeores.2009.11.008>
- Eichelberger JC, Carrigan CR, Westrich HR, Price RH (1986) Non-explosive silicic volcanism. *Nature* 323:598–602. <https://doi.org/10.1038/323598a0>
- Geschwind C-H, Rutherford MJ (1995) Crystallization of microlites during magma ascent: the fluid mechanics of 1980–1986 eruptions at Mount St. Helens. *Bull Volcanol* 57:356–370. <https://doi.org/10.1007/BF00301293>
- Ghiorso MS, Gualda GAR (2015) An H<sub>2</sub>O-CO<sub>2</sub> mixed fluid saturated model compatible with rhyolite-MELTS. *Contrib Miner Petrol* 169:53. <https://doi.org/10.1007/s00410-015-1141-8>
- Gualda GAR, Ghiorso MS, Lemons RV, Carley TL (2012) Rhyolite-MELTS: A modified calibration of MELTS optimized for silica-rich, fluid-bearing magmatic systems. *J Petrol* 53:875–890. <https://doi.org/10.1093/petrology/egr080>
- Hammer JE (2004) Crystal nucleation in hydrous rhyolite: experimental data applied to classical theory. *Am Miner* 89(11–12):1673–1679. <https://doi.org/10.2138/am-2004-11-1212>
- Hammer JE, Rutherford MJ (2002) An experimental study of the kinetics of decompression-induced crystallization in silicic melt. *J Geophys Res*. <https://doi.org/10.1029/2001JB000281>
- Jaupart C, Allegre C (1991) Gas content, eruption rate and instabilities of eruption regime in silicic volcanoes. *Earth Planet Sci Lett* 102:413–429. [https://doi.org/10.1016/0012-821X\(91\)90032-D](https://doi.org/10.1016/0012-821X(91)90032-D)
- La Spina G, Arzilli F, Llewellyn EW, Burton MR, Clark AB, Vitturi MDM, Polacci M, Hartley ME, Di Genova D, Mader HM (2021) Explosivity of basaltic lava fountains is controlled by magma rheology, ascent rate and outgassing. *Earth Planet Sci Lett* 553:116658. <https://doi.org/10.1016/j.epsl.2020.116658>
- La Spina G, Burton M, de' Michieli Vitturi M, Arzilli F, (2016) Role of syn-eruptive plagioclase disequilibrium crystallization in basaltic magma ascent dynamics. *Nat Commun* 7:13402. <https://doi.org/10.1038/ncomms13402>
- Lange RA, Frey HM, Hector J (2009) A thermodynamic model for the plagioclase-liquid hygrometer/thermometer. *Am Miner* 94:494–506. <https://doi.org/10.2138/am.2009.3011>
- Liu Y, Anderson AT, Wilson CJN (2007) Melt pockets in phenocrysts and decompression rates of silicic magmas before fragmentation. *J Geophys Res* 112:B06204. <https://doi.org/10.1029/2006JB004500>
- Lohmar S (2008) Petrología de las ignimbritas Lican y Pucon (volcan Villarrica) y Curacautín (volcan Llaima) en los Andes del sur de Chile. Dissertation, University of Chile
- Mangan M, Sisson T (2000) Delayed, disequilibrium degassing in rhyolitic magma: decompression experiments and implications for explosive volcanism. *Earth Planet Sci Lett* 183:441–455. [https://doi.org/10.1016/S0012-821X\(00\)00299-5](https://doi.org/10.1016/S0012-821X(00)00299-5)
- Marsh BD (1988) Crystal size distribution (CSD) in rocks and the kinetics and dynamics of crystallization: I. Theory. *Contrib Miner Petrol* 99:277–291. <https://doi.org/10.1007/BF00375362>
- Marshall AA, Brand BD, Martínez V, Bowers J, Walker M, Wanless VD, Andrews BJ, Manga M, Valdivia P, Giordano G (2022a) The mafic Curacautín ignimbrite of Llaima volcano, Chile. *J Volcanol Geotherm Res* 421:107418. <https://doi.org/10.1016/j.jvolgeores.2021.107418>
- Marshall AA, Manga M, Brand BD, Andrews BJ (2022b) Autobrecciation and fusing of mafic magma preceding explosive eruptions. *Geology* 50(10):1177–1181. <https://doi.org/10.1130/G50180.1>
- Mastin LG, Ghiorso MS (2000) A numerical program for steady-state flow of magma-gas mixtures through vertical eruptive conduits. U.S. Geological Survey Open-File Report 2000–209, p 66. <https://doi.org/10.3133/ofr00209>
- Mastin LG, Ghiorso MS (2001) Adiabatic temperature changes of magma-gas mixtures during ascent and eruption. *Contrib Miner Petrol* 141:307–321. <https://doi.org/10.1007/s004100000210>
- Moran SC, Malone SD, Qamar AI, Thelen WA, Wright AK, Caplan-Auerbach J (2008) Seismicity associated with renewed dome building at Mount St. Helens, 2004–2005. In: Sherrod DR, Scott WE, Stauffer PH (eds) *A Volcano Rekindled: the renewed eruption of Mount St. Helens, 2004–2005*. U.S. Geological Survey Professional Paper, vol 1750, pp 27–54. <https://doi.org/10.3133/pp17502>
- Murch AP, Cole PD (2019) Using microlites to gain insights into ascent conditions of differing styles of volcanism at Soufrière Hills Volcano. *J Volcanol Geotherm Res* 384:221–231. <https://doi.org/10.1016/j.jvolgeores.2019.07.022>
- Myers ML, Wallace PJ, Wilson CJN, Morter BK, Swallow EJ (2016) Prolonged ascent and episodic venting of discrete magma batches at the onset of the Huckleberry Ridge supereruption, Yellowstone. *Earth Planet Sci Lett* 451:285–297. <https://doi.org/10.1016/j.epsl.2016.07.023>
- Myers ML, Wallace PJ, Wilson CJN, Watkins JM, Liu Y (2018) Ascent rates of rhyolitic magma at the onset of caldera-forming eruptions. *Am Miner* 103(6):952–965. <https://doi.org/10.2138/am-2018-6225>
- Naranjo JA, Moreno H (2005) Geología del volcán Llaima, Región de la Araucanía. Servicio Nacional de Geología y Minería, Carta Geológica de Chile, Serie Geología Básica 88:1–33. Escala 1:50,000. <https://www.scribd.com/document/385589999/Geologia-Volcan-Llaima-pdf>
- Naranjo JA, Moreno H (1991) Actividad explosiva postglacial en el volcán Llaima, Andes del Sur (38°45'S). *Rev Geol Chile* 18(1):69–80. <https://doi.org/10.5027/andgeoV18n1-a06>
- Putirka KD (2008) Thermometers and barometers for volcanic systems. *Rev Miner Geochem* 69:61–120. <https://doi.org/10.2138/rmg.2008.69.3>
- Rowe MC, Carey RJ, White JDL, Kilgour G, Hughes E, Ellis B, Rosseel J-B, Segovia A (2021) Tarawera 1886: an integrated review of volcanological and geochemical characteristics of complex basaltic eruption. *N Z J Geol Geophys*. <https://doi.org/10.1080/00288306.2021.1914118>
- Rusiecka MK, Bilodeau M, Baker DR (2020) Quantification of nucleation delay in magmatic systems: experimental and theoretical approach. *Contrib Miner Petrol* 175:47. <https://doi.org/10.1007/s00410-020-01682.4>
- Rutherford MJ, Hill PM (1993) Magma ascent rates from amphibole breakdown: an experimental study applied to the 1980–1986 Mount St. Helens eruptions. *J Geophys Res* 98(B11):19667–19684. <https://doi.org/10.1029/93JB01613>
- Sable JE, Houghton BF, Del Carlo P, Coltelli M (2006) Changing conditions of magma ascent and fragmentation during the Etna 122 BC basaltic Plinian eruption: evidence from clast microtextures. *J Volcanol Geotherm Res* 158:333–354. <https://doi.org/10.1016/j.jvolgeores.2006.07.006>
- Sable JE, Houghton BF, Wilson CJN, Carey RJ (2009) Eruption mechanisms during the climax of the Tarawera 1886 basaltic Plinian eruption inferred from microtextural characteristics of the deposits. In: Thordarson T, Self S, Larsen G, Rowland SK, Hoskuldsson A (eds) *Studies in volcanology: the legacy of George Walker*, vol 2. Special Publications of IAVCEI, pp 129–154. <https://doi.org/10.1144/IAVCEI002.7>

- Schindlbeck JC, Freundt A, Kutterolf S (2014) Major changes in the post-glacial evolution of magmatic compositions and pre-eruptive conditions at Llaima volcano, Andean Southern Volcanic Zone, Chile. *Bull Volcanol* 76:830. <https://doi.org/10.1007/s00445-014-0830-x>
- Shea T (2017) Bubble nucleation in magmas: a dominantly heterogeneous process? *J Volcanol Geotherm Res* 343:155–170. <https://doi.org/10.1016/j.jvolgeores.2017.06.025>
- Shea T, Hammer JE (2013) Kinetics of cooling- and decompression-induced crystallization in hydrous mafic-intermediate magmas. *J Volcanol Geotherm Res* 260:127–145. <https://doi.org/10.1016/j.jvolgeores.2013.04.018>
- Szramek L, Gardner JE, Larsen J (2006) Degassing and microlite crystallization of basaltic andesite magma erupting at Arenal Volcano, Costa Rica. *J Volcanol Geotherm Res* 157:182–201. <https://doi.org/10.1016/j.jvolgeores.2006.03.039>
- Thelen WA, Crosson RS, Creagor KC (2008) Absolute and relative locations of earthquakes at Mount St. Helens, Washington, using continuous data: implications for magmatic processes. In: Sherrod DR, Scott WE, Stauffer PH (eds) *A Volcano Rekindled: the renewed eruption of Mount St. Helens, 2004–2005*. U.S. Geological Survey Professional Paper, vol 1750, pp 71–95. <https://doi.org/10.3133/pp17504>
- Toramaru A (2006) BND (bubble number density) decompression rate meter for explosive volcanic eruptions. *J Volcanol Geotherm Res* 154:303–316. <https://doi.org/10.1016/j.jvolgeores.2006.03.027>
- Toramaru A, Noguchi S, Oyoshihara S, Tsune A (2008) MND (microlite number density) water exsolution rate meter. *J Volcanol Geotherm Res* 175(1–2):156–167. <https://doi.org/10.1016/j.jvolgeores.2008.03.035>
- Valdivia P, Marshall AA, Manga M, Brand BD, Huber C (2022) Mafic explosive volcanism at Llaima volcano: 3D X-ray microtomography reconstruction of pyroclasts to constrain shallow conduit processes. *Bull Volcanol* 84(2). <https://doi.org/10.1007/s00445-021-01514-8>
- Vetere F, Petrelli M, Perugini D, Haselbach S, Morgavi D, Pisello A, Iezzi G, Holtz F (2021) Rheological evolution of eruptible Basaltic-Andesite Magmas under dynamic conditions: the importance of plagioclase growth rates. *J Volcanol Geotherm Res* 420:107411. <https://doi.org/10.1016/j.jvolgeores.2021.107411>
- Vinkler AP, Cashman KV, Giordano G, Groppelli G (2012) evolution of the mafic Villa Senni caldera-forming eruption at Colli Albani volcano, Italy, indicated by textural analysis of juvenile fragments. *J Volcanol Geotherm Res* 235–236:37–54. <https://doi.org/10.1016/j.jvolgeores.2012.03.006>
- Vona A, Romano C, Dingwell DB, Giordano D (2011) The rheology of crystal-bearing basaltic magmas from Stromboli and Etna. *Geochim Cosmochim Acta* 75:3214–3236. <https://doi.org/10.1016/j.gca.2011.03.031>
- Waters LE, Andrews BJ, Lange RA (2015) Rapid crystallization of plagioclase phenocrysts in silicic melts during fluid-saturated ascent: phase equilibrium and decompression experiments. *J Petrol* 56:981–1006. <https://doi.org/10.1093/petrology/egv025>

**Publisher's Note** Springer Nature remains neutral with regard to jurisdictional claims in published maps and institutional affiliations.